recycling

MDPI

Article

The Use of MSWI Fly Ash in Promoting Low-Titanium Slag Activation for Use in Low-Carbon Cementitious Materials

Bo Su [1,2,3], Jie Chi [2,3], Siqi Zhang [1,2,3,*], Jia Li [1,2,3], Keqing Li [2,3], Xingyang Xu [2,3] and Wen Ni [2,3]

[1] Institute of Minerals Resources, University of Science and Technology Beijing, Beijing 100083, China; ustb_subo@163.com (B.S.)
[2] School of Civil and Resource Engineering, University of Science and Technology Beijing, Beijing 100083, China
[3] China-Zambia Belt and Road Joint Laboratory on Green and Safe Development of Mineral Resources, School of Resources and Safety Engineering, University of Science and Technology Beijing, Beijing 100083, China
* Correspondence: zsq2017@ustb.edu.cn

Abstract

A quaternary solid-waste-based binder was prepared from low-titanium slag, municipal solid waste incineration (MSWI) fly ash, steel slag, and flue-gas desulfurization gypsum (FGDG) to clarify the activating effect of MSWI fly ash on low-titanium slag and its influence on hydrate evolution. Unlike conventional solid-waste-based binders in which MSWI fly ash is mainly regarded as a hazardous residue requiring stabilization, this study demonstrates its specific role as a Ca-rich alkaline activator for promoting low-titanium slag depolymerization and coordinated hydrate formation. The results showed that the compressive strength first increased and then decreased with increasing MSWI fly ash content. Considering both strength development and MSWI fly ash utilization, the optimum mixture was identified as low-titanium slag:MSWI fly ash:steel slag:FGDG = 43.0:17.2:25.8:14.0, with compressive strengths of 9.51 and 46.32 MPa at 3 and 90 d, respectively. These values corresponded to 5.66 and 1.04 times those of the reference mixture without MSWI fly ash, respectively. Ettringite and C-(A)-S-H gel were the main strength-contributing hydration products, while Friedel's salt was identified as a chloride-bearing AFm phase. Moderate MSWI fly ash addition promoted alkaline activation and low-titanium slag depolymerization, leading to increased formation of ettringite, C-(A)-S-H gel, and Friedel's salt, which contributed to improved compressive strength. In contrast, excessive MSWI fly ash disturbed the Ca-Si-Al balance and inhibited effective hydrate formation. These results demonstrate that MSWI fly ash can serve as an effective Ca-rich activator for low-titanium-slag-based low-carbon cementitious materials and provide a feasible route for the synergistic utilization of multiple solid wastes.

Keywords: low-titanium slag; MSWI fly ash; composite activation; low-carbon cementitious materials

Check for updates

Academic Editor: Michele John

Received: 3 April 2026
Revised: 20 May 2026
Accepted: 22 May 2026
Published: 27 May 2026

Copyright: © 2026 by the authors. Licensee MDPI, Basel, Switzerland. This article is an open access article distributed under the terms and conditions of the Creative Commons Attribution (CC BY) license.

1. Introduction

The decarbonization of cementitious materials has become a central challenge in sustainable construction because conventional Portland cement production is inherently energy intensive, resource intensive, and carbon intensive. Current assessments indicate that the direct emissions intensity of cement production remains close to 0.6 t CO_2 per tonne of cement, which means that substantial carbon mitigation will depend not only on process optimization, but also on the replacement of clinker by low-carbon alternative binders derived from industrial by-products [1]. In this context, the development of cementitious

materials based on solid wastes is not merely a disposal strategy, but an essential pathway toward resource-efficient and low-carbon material systems.

Among the various waste streams available for binder design, steel slag and FGDG have been widely recognized as functionally valuable constituents because they can respectively provide Ca-rich alkaline phases and sulfate for hydrate formation. By contrast, the resource utilization of MSWI fly ash remains far more challenging owing to its complex chemistry, high alkalinity, and the coexistence of soluble salts and hazardous species. Recent reviews have shown that the annual generation of MSWI fly ash in China has exceeded 10 million tonnes and that the dominant management route is still solidification/stabilization followed by landfill disposal [2]. Although this pathway can achieve short-term hazard control, it does not fully exploit the intrinsic chemical value of MSWI fly ash in low-carbon cementitious systems. From a materials perspective, the high Ca content and alkalinity of MSWI fly ash suggest that it may act not only as a residue requiring stabilization, but also as a potentially reactive Ca-rich component in multi-solid-waste binders. Moreover, chlorides and soluble salts in MSWI fly ash can modify the pore-solution ionic environment and influence the dissolution and reorganization of the Ca-Si-Al network in low-titanium slag. Chloride may react with Ca- and Al-bearing species to form Friedel's salt [3,4], whereas excessive soluble salts can disturb the Ca-Si-Al-S balance and hinder the sustained formation of ettringite and C-(A)-S-H gel [5]. In addition, the potential leaching of heavy metals from MSWI fly ash remains a critical barrier to its acceptance in construction materials [6,7]. Therefore, the coordinated use of MSWI fly ash in low-carbon cementitious systems should not only promote slag activation and hydrate formation, but also ensure the immobilization of hazardous elements through physical encapsulation and chemical binding within hydration products.

Low-titanium slag is another underutilized by-product with considerable potential for cementitious applications. Publicly available statistics are commonly reported for titanium-bearing blast furnace slag as a whole rather than for low-titanium slag alone, but recent studies consistently indicate that China generates approximately 7 million tonnes of titanium-bearing blast furnace slag annually, with accumulated stockpiles already exceeding 100 million tonnes, while the overall utilization rate remains below 3% [8]. Despite its Ca-Si-Al-bearing composition, low-titanium slag exhibits relatively low intrinsic hydraulic activity compared with conventional blast furnace slag, and its efficient utilization therefore depends on the establishment of an appropriate activation environment [9]. This issue is particularly important for regions such as southwest China, where vanadium titanomagnetite smelting produces large quantities of titanium-bearing slags but high-value utilization routes remain limited.

From the perspective of binder chemistry, a key unresolved issue is how MSWI fly ash participates in the activation of low-reactivity low-titanium slag, rather than only acting as a waste component requiring stabilization or as a general alkaline additive. This issue is particularly important because low-titanium slag contains Ca-Si-Al-bearing phases but exhibits limited intrinsic hydraulic activity, and its efficient utilization depends on the construction of a suitable alkaline-sulfate reaction environment. The quaternary system composed of low-titanium slag, steel slag, FGDG, and MSWI fly ash differs from conventional multi-solid-waste binders in both composition and reaction pathway. In this system, low-titanium slag serves as the principal aluminosilicate precursor, MSWI fly ash provides Ca-rich alkaline species to promote slag depolymerization, steel slag supplies additional reactive Ca-bearing phases, and FGDG continuously provides sulfate for ettringite formation. This design enables the coupled regulation of Ca supply, sulfate activation, aluminosilicate network dissolution, and hydrate evolution within an all-solid-waste matrix. Its potential application is also closely related to cemented paste backfill, where reducing

cement consumption and increasing regional solid-waste utilization are both critical for engineering and environmental performance [10]. However, the dosage-dependent activation role of MSWI fly ash in low-titanium-slag-based cementitious systems remains insufficiently clarified. In particular, how MSWI fly ash-derived Ca-rich alkaline species regulate pore-solution chemistry, promote the depolymerization of the low-reactivity Ca-Si-Al network, and affect the subsequent formation of ettringite and C-(A)-S-H gel has not been systematically revealed [11].

Accordingly, this study developed a quaternary binder system composed of low-titanium slag, MSWI fly ash, steel slag, and FGDG. The objectives were to determine the optimum MSWI fly ash dosage, clarify its activating effect on low-titanium slag, and elucidate the associated hydration mechanism. To this end, compressive strength at different curing ages was combined with the efficacy coefficient method for mixture optimization, while the hydration products, heat evolution, elemental chemical-state changes, and microstructural development were systematically characterized by XRD, FT-IR, TG-DTG, isothermal calorimetry, XPS, and SEM. This work is expected to provide both a mechanistic basis for the design of low-titanium-slag-based low-carbon binders and a feasible route for the coordinated high-value utilization of metallurgical solid wastes and MSWI fly ash.

2. Results and Discussion

2.1. Effect of MSWI Fly Ash Content on the Performance of the Binder

As shown in Figure 1, the compressive strength of all mixtures increased progressively with curing age, reflecting the continuous hydration and gradual microstructural densification of the binder system. With the combined content of low-titanium slag and FGDG fixed, progressively increasing the replacement of steel slag by MSWI fly ash led to a consistent strength evolution pattern at all ages, characterized by an initial increase followed by a decline. Specifically, all fly ash-containing mixtures (G2–G6) exhibited higher 3 d compressive strength than the MSWI fly ash-free mixture (G1), indicating that MSWI fly ash was more effective than steel slag in establishing an alkaline reaction environment at the early stage, thereby facilitating the initial activation of the system. This confirms that the incorporation of MSWI fly ash can effectively enhance early-age strength while promoting its synergistic utilization in the quaternary binder. However, the subsequent decrease in strength at higher MSWI fly ash contents also reveals the limited substitution capacity of fly ash for steel slag. Although both materials contribute to the alkalinity required for precursor activation, steel slag additionally contains reactive silicate phases such as C_3S and C_2S, which can hydrate to form C-S-H gel and thus play a crucial role in matrix consolidation and strength development [12]. In contrast, MSWI fly ash, despite its high CaO content, cannot provide the same hydration contribution. Consequently, excessive MSWI fly ash addition accompanied by insufficient steel slag weakened the formation of strength-bearing hydrates, resulting in reduced compressive strength. Notably, from the perspective of long-term performance, all MSWI fly ash-containing mixtures achieved the target strength of 30 MPa at 90 d, and the mixtures with moderate MSWI fly ash contents, particularly G2 and G3, showed superior 90 d strength to G1, with increases of 0.66% and 4.31%, respectively. These results demonstrate that an appropriate dosage of MSWI fly ash not only promotes early hydration activation but also contributes positively to the long-term mechanical performance of the binder system.

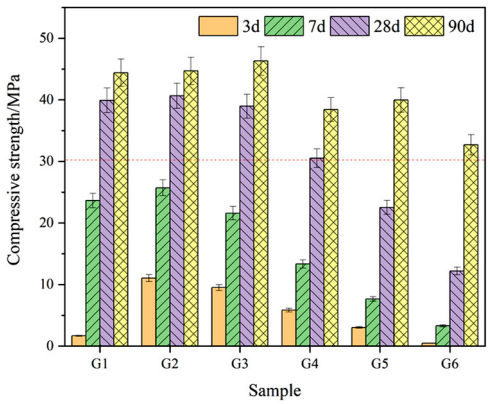


Figure 1. Compressive Strength of Low-Titanium Slag-Based Quaternary Cementitious System.

2.2. Determination of the Optimal Mixture Proportion of the MSWI Fly Ash-Low-Titanium Slag-Based Binder Based on the Efficacy Coefficient Method

Figure 1 shows that the compressive strength of the quaternary binder system exhibited a consistent increase-then-decrease trend with increasing MSWI fly ash content at all curing ages, although all mixtures still exceeded 30 MPa at 90 d. The optimum MSWI fly ash dosage was clearly age-dependent. G2 containing 8.6% MSWI fly ash achieved the highest strengths at 3–28 d, with values of 11.05, 25.71, and 40.66 MPa at 3, 7, and 28 d, respectively, whereas further increasing the MSWI fly ash content to 17.2–34.4% resulted in a progressive strength reduction. In contrast, G3 with 17.2% MSWI fly ash exhibited the highest 90 d strength of 46.32 MPa. These results indicate that MSWI fly ash exerts a time-dependent effect on strength development, and its optimum dosage should be selected by balancing early-age performance and later-age strength gain.

To further identify the optimum formulation, the efficacy coefficient method was applied using the compressive strengths at 3, 7, 28, and 90 d as integrated evaluation indices. The maximum strength at each curing age was assigned an efficacy coefficient of 1, and the remaining values were normalized as the ratio of the measured strength to the corresponding maximum value. The overall efficacy coefficient (OEC) was then calculated as the geometric mean of the four individual efficacy coefficients. In Table 1, d_1, d_2, d_3, and d_4 represent the individual efficacy coefficients at 3, 7, 28, and 90 d, respectively, and D denotes the overall efficacy coefficient (OEC). As listed in Table 1, G2 exhibited the highest overall efficacy coefficient (0.99), indicating the best comprehensive mechanical performance among the tested mixtures. However, G3 achieved the highest 90 d compressive strength and incorporated twice the MSWI fly ash content of G2, while still maintaining satisfactory early-age and 28 d strength. Therefore, considering both mechanical performance and the objective of increasing MSWI fly ash utilization, G3 was selected as the preferred formulation for the quaternary binder system. The corresponding mix proportion of low-titanium slag, MSWI fly ash, steel slag, and gypsum was 43.0:17.2:25.8:14.0.

Table 1. Efficacy Coefficient Analysis of Formulation Schemes.

Sample	Compressive Strength (MPa)				EC				OEC
	3 d	7 d	28 d	90 d	d_1	d_2	d_3	d_4	D
G1	1.68	23.66	39.94	44.41	0.15	0.92	0.98	0.96	0.60
G2	11.05	25.71	40.66	44.70	1.00	1.00	1.00	0.97	0.99
G3	9.51	21.60	38.98	46.32	0.86	0.84	0.96	1	0.91
G4	5.85	13.33	30.54	38.43	0.53	0.52	0.75	0.83	0.64
G5	3.04	7.65	22.55	39.98	0.27	0.30	0.55	0.86	0.44
G6	0.48	3.29	12.21	32.70	0.04	0.13	0.30	0.71	0.18

2.3. Hydration Mechanism of the MSWI Fly Ash-Low-Titanium Slag Quaternary Binder System

2.3.1. Hydration Heat Evolution Analysis of the Hydration Reaction

As shown in Figure 2a, the cumulative heat release of all mixtures increased continuously with hydration time, but clear differences were observed among the formulations. G3 exhibited the highest cumulative heat release throughout the later hydration period, indicating the greatest overall hydration degree and the most sustained reaction process. This result agrees well with its superior long-term compressive strength, confirming that a moderate dosage of MSWI fly ash was beneficial to prolonged hydrate formation and matrix development. In contrast, G6 showed the lowest cumulative heat release, suggesting that excessive MSWI fly ash suppressed the overall hydration process. This behavior was mainly attributed to the disturbance of the Ca-Si-Al balance and the reduction in the proportion of effective reactive precursors at high MSWI fly ash contents, which limited the continued formation of hydration products.

The heat-flow curves in Figure 2b further reveal that all mixtures exhibited a typical multi-stage exothermic pattern. A sharp initial peak appeared within 0.1–0.8 h, corresponding to the rapid wetting, dissolution, and early reaction of highly reactive Ca-bearing phases. A second weak peak was observed at around 8 h and was mainly associated with the sulfate–aluminate reaction and ettringite formation [13]. At this stage, G2 and G3 showed relatively higher heat flow than the other mixtures, indicating that a moderate amount of MSWI fly ash promoted the establishment of a favorable alkaline environment and accelerated the release of reactive silicate and aluminate species from low-titanium slag. A broad late exothermic stage appeared over approximately 60–160 h, which was associated with the continued hydration of relatively slow-reacting phases and the sustained formation of C-(A)-S-H gel [14]. Overall, the results demonstrate that MSWI fly ash plays a dosage-dependent role in the quaternary binder system: an appropriate incorporation level promotes both early activation and sustained hydration, whereas excessive addition weakens reaction continuity and is unfavorable for strength development.

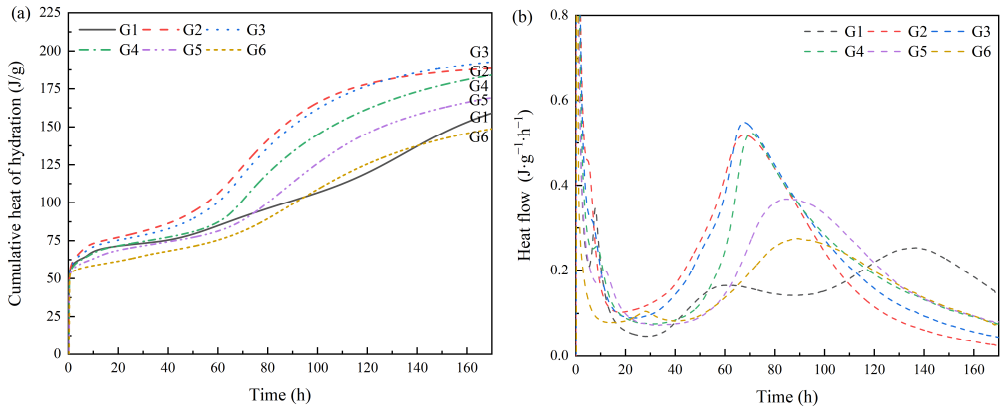


Figure 2. Hydration heat evolution of the quaternary binder systems: (**a**) cumulative heat release; (**b**) heat flow.

2.3.2. XRD Analysis of Hydration Products

Figure 3 shows that the hydrated pastes were mainly composed of ettringite, Friedel's salt, $Ca(OH)_2$, residual C_2S, C_3S and $CaSO_4 \cdot 2H_2O$, together with the inert RO phase. In addition, a weak diffuse hump gradually appeared in the 2θ range of 29–35°, indicating the formation of poorly crystalline C-(A)-S-H gel. At 3 d, only weak ettringite reflections were detected, confirming that hydration had already been initiated at the early stage. With increasing curing age, the ettringite peaks became progressively stronger, especially from 7 to 28 d, suggesting continuous sulfate consumption and sustained crystallization

of ettringite. Meanwhile, the amorphous hump became more evident at later ages, indicating the gradual accumulation of C-(A)-S-H gel. These results suggest that the strength development of the quaternary system was governed by the sequential formation of an ettringite-dominated early skeleton and a C-(A)-S-H-dominated later binding network.

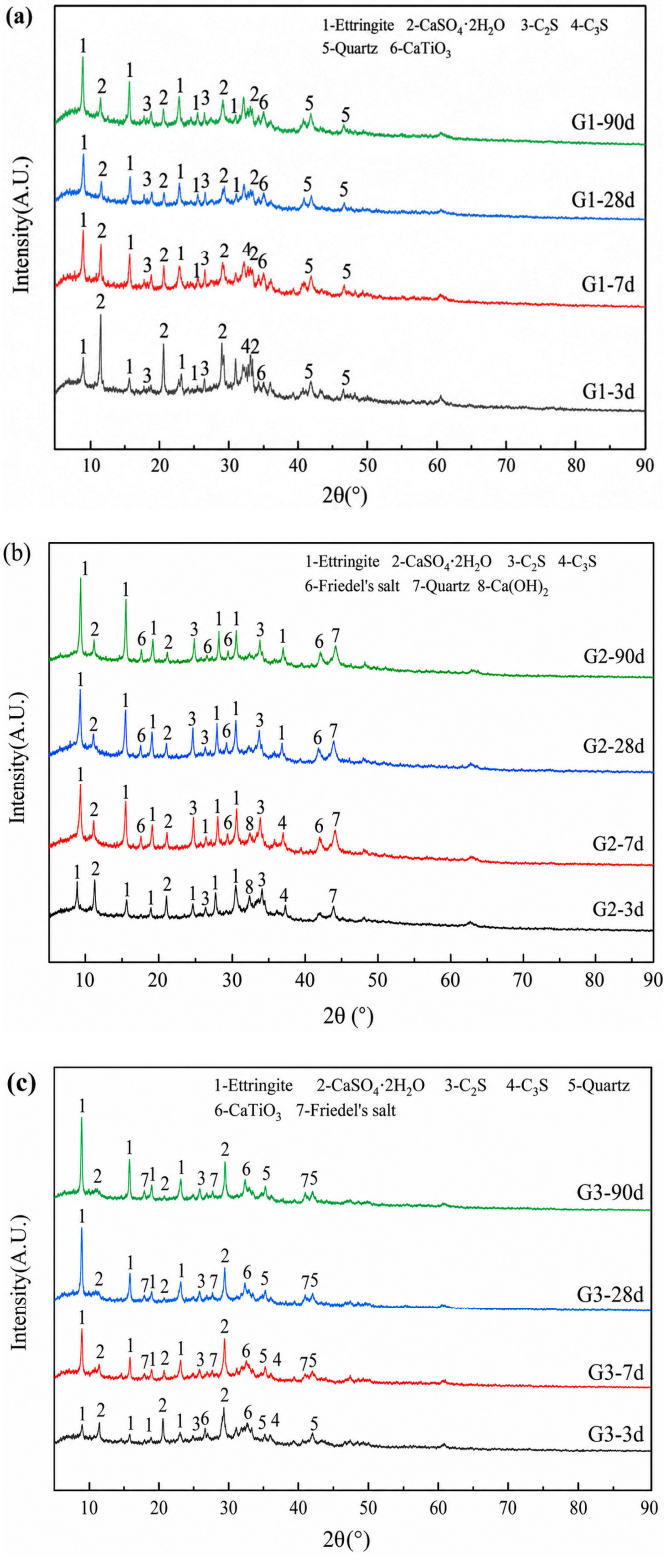


Figure 3. *Cont*.

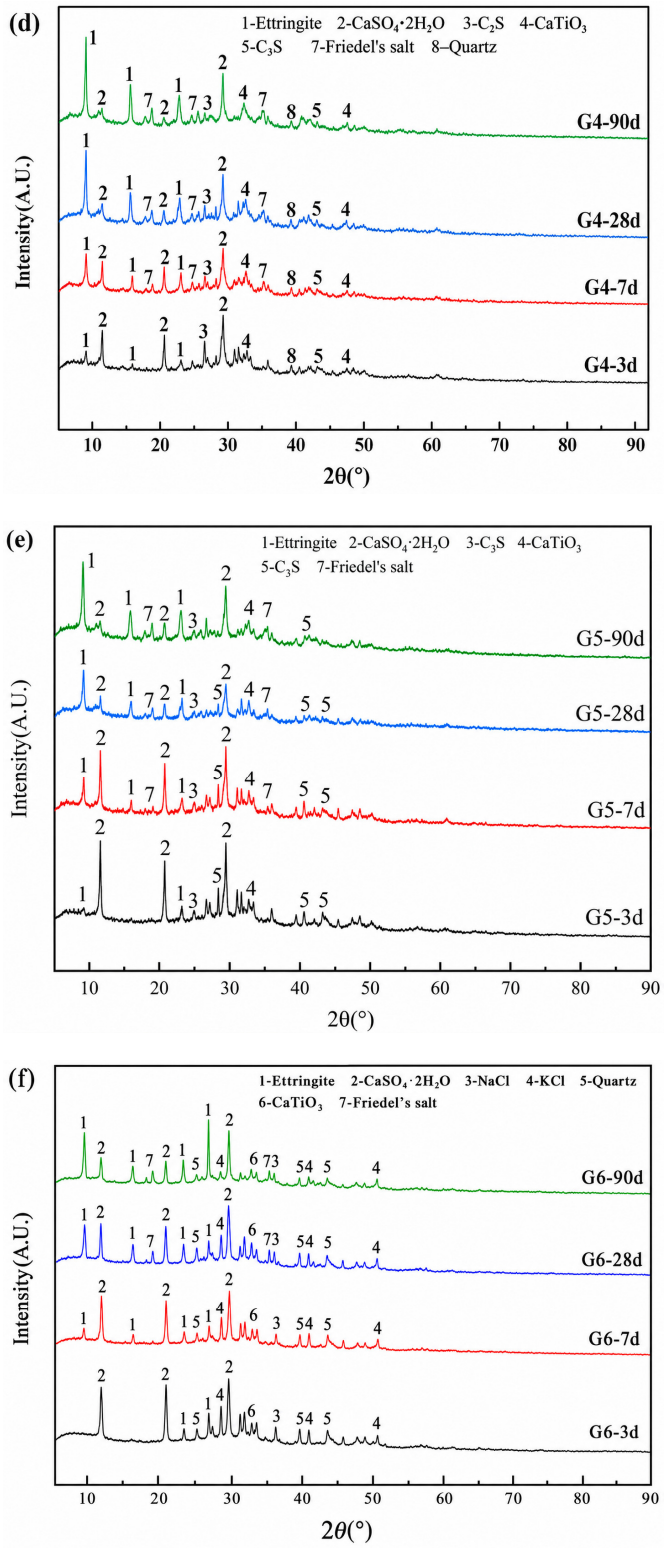


Figure 3. XRD patterns of the quaternary binder systems at different curing ages: (**a**) G1; (**b**) G2; (**c**) G3; (**d**) G4; (**e**) G5; (**f**) G6.

The phase evolution also revealed a clear dosage-dependent role of MSWI fly ash. In G2 and G3, the C_3S reflections disappeared by 28 d, indicating more complete hydration of reactive silicate phases, which is consistent with their superior mechanical performance. By contrast, C_2S decreased more gradually and remained detectable even at 90 d, confirming its contribution to long-term gel formation and later-age strength gain. $Ca(OH)_2$ was mainly observed at 3–7 d and disappeared at 28 d in G1–G4, implying that the early-

generated alkalinity was subsequently consumed by the activation of low-titanium slag and the formation of secondary hydrates. The progressive attenuation of $CaSO_4 \cdot 2H_2O$ further confirms its continuous participation in ettringite formation, particularly during the 7–28 d interval when strength increased most rapidly. A characteristic reflection of Friedel's salt was also identified, demonstrating that chloride released from MSWI fly ash was chemically incorporated into a stable AFm-type phase. Therefore, the XRD results indicate that an appropriate amount of MSWI fly ash not only promotes the hydration of reactive silicate phases and the formation of ettringite and C-(A)-S-H, but also facilitates chloride immobilization through Friedel's salt formation, which is a key advantage of this quaternary binder system.

Figure 4 compares the phase assemblages of G1 without MSWI fly ash, G3 with the optimum proportion, and G6 with the highest MSWI fly ash dosage at 3 and 28 d. At both curing ages, G3 exhibited the most favorable hydration characteristics, as evidenced by the stronger ettringite reflections, the more discernible diffuse hump assigned to poorly crystalline C-(A)-S-H gel, and the lower residual gypsum peak intensity relative to G1 and G6. These features indicate that an appropriate amount of MSWI fly ash promoted sulfate consumption and enhanced the coupled formation of ettringite and C-(A)-S-H, which is consistent with the superior mechanical performance of G3. This result suggests that moderate MSWI fly ash addition does not merely provide alkalinity, but also optimizes the reaction pathway by accelerating the dissolution of reactive Si- and Al-bearing phases in the low-titanium slag-based system and promoting the development of a dual hydrate framework composed of ettringite and C-(A)-S-H.

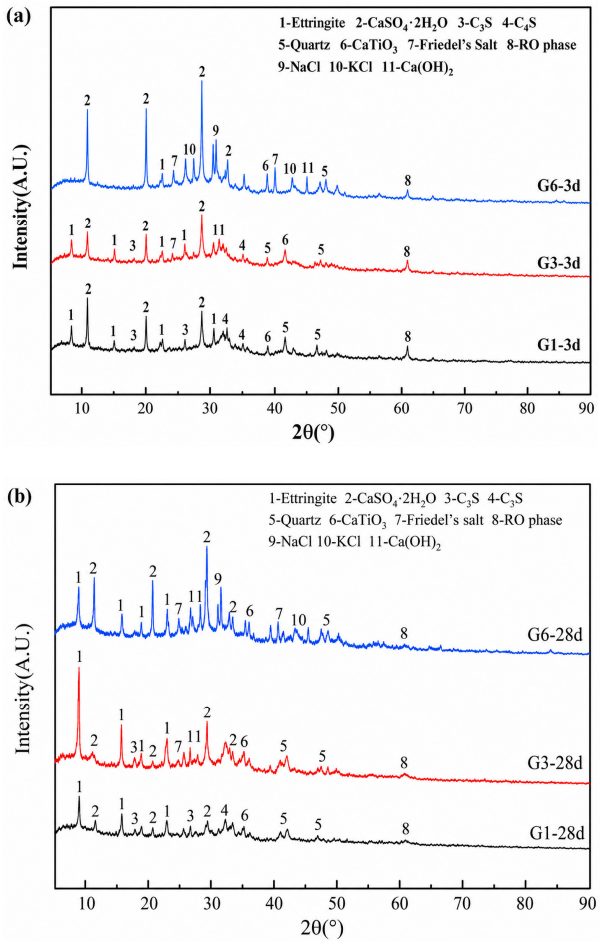


Figure 4. XRD comparison of the MSWI fly ash-low-titanium slag-based quaternary binder systems at different curing ages: (**a**) 3 d; (**b**) 28 d.

By contrast, G6 showed clear signs of hydration inhibition. The weaker ettringite peaks, the absence of an obvious C-(A)-S-H amorphous hump, and the higher residual gypsum intensity indicate that excessive MSWI fly ash suppressed the effective progression of hydration. This behavior can be attributed to the excessive chloride and Ca-rich components introduced by high MSWI fly ash addition. On the one hand, chloride preferentially reacted with aluminate species to form Friedel's salt, thereby consuming reactive Al and weakening ettringite formation. On the other hand, excess CaO disturbed the Ca-Si-Al balance of the system and was unfavorable for the sustained growth of a dense C-(A)-S-H network. Therefore, the XRD comparison confirms that the beneficial effect of MSWI fly ash is strongly dosage-dependent: appropriate incorporation enhances hydrate evolution and structural build-up, whereas excessive addition shifts the system toward chloride binding and incomplete hydration, ultimately impairing later-age performance.

2.3.3. FT-IR Analysis

Figure 5 further clarifies the evolution of the hydration products, particularly the poorly crystalline C-(A)-S-H gel that cannot be fully resolved by XRD. All mixtures exhibited similar band positions, indicating comparable types of hydration products, whereas the band intensity evolved markedly with curing age, reflecting differences in hydration degree and product accumulation. The broad bands at approximately 3400 and 1600 cm^{-1} were assigned to the O-H stretching and H-O-H bending vibrations of bound water, mainly associated with ettringite and C-(A)-S-H gel [15,16]. Their progressive enhancement from 3 to 90 d indicates the continuous formation of hydrated phases. The band near 1110 cm^{-1} corresponds to S-O asymmetric stretching, arising from sulfate-bearing phases such as gypsum and ettringite [17], while the band around 970 cm^{-1} is attributed to Si-O asymmetric stretching in silicate tetrahedra [18]. In addition, the bands near 670, 600, and 510 cm^{-1} are assigned to Si-O-(Al) bending vibrations, confirming the gradual development of aluminosilicate hydrate structures [19,20]. The bands at approximately 1450–1470 cm^{-1} and 875 cm^{-1} were assigned to the characteristic vibrations of CO_3^{2-}, indicating the presence of minor carbonate species, mainly $CaCO_3$. These carbonate signals may be related to slight surface carbonation during curing, drying, or sample handling [21]. Overall, the FT-IR results indicate that the quaternary system underwent continuous hydration, accompanied by sustained formation and structural evolution of ettringite and C-(A)-S-H gel.

The variation in MSWI fly ash content further affected the development of hydration-related bands. Among the representative mixtures, G3 showed the strongest hydration-related bands and the most evident evolution of the O-H, H-O-H, and Si-O-(Al) vibrations, indicating the highest degree of hydrate accumulation and polymerized gel development. This result is consistent with the XRD and strength results, confirming that an appropriate amount of MSWI fly ash effectively promoted both early hydration and later structural build-up. By contrast, G6 exhibited weaker hydration-related bands, suggesting a lower extent of hydrate formation and a less developed gel network. Therefore, the FT-IR analysis further demonstrates that moderate MSWI fly ash incorporation optimizes the hydration pathway of the low-titanium slag-based quaternary binder, whereas excessive addition suppresses effective gel formation and is unfavorable for long-term performance.

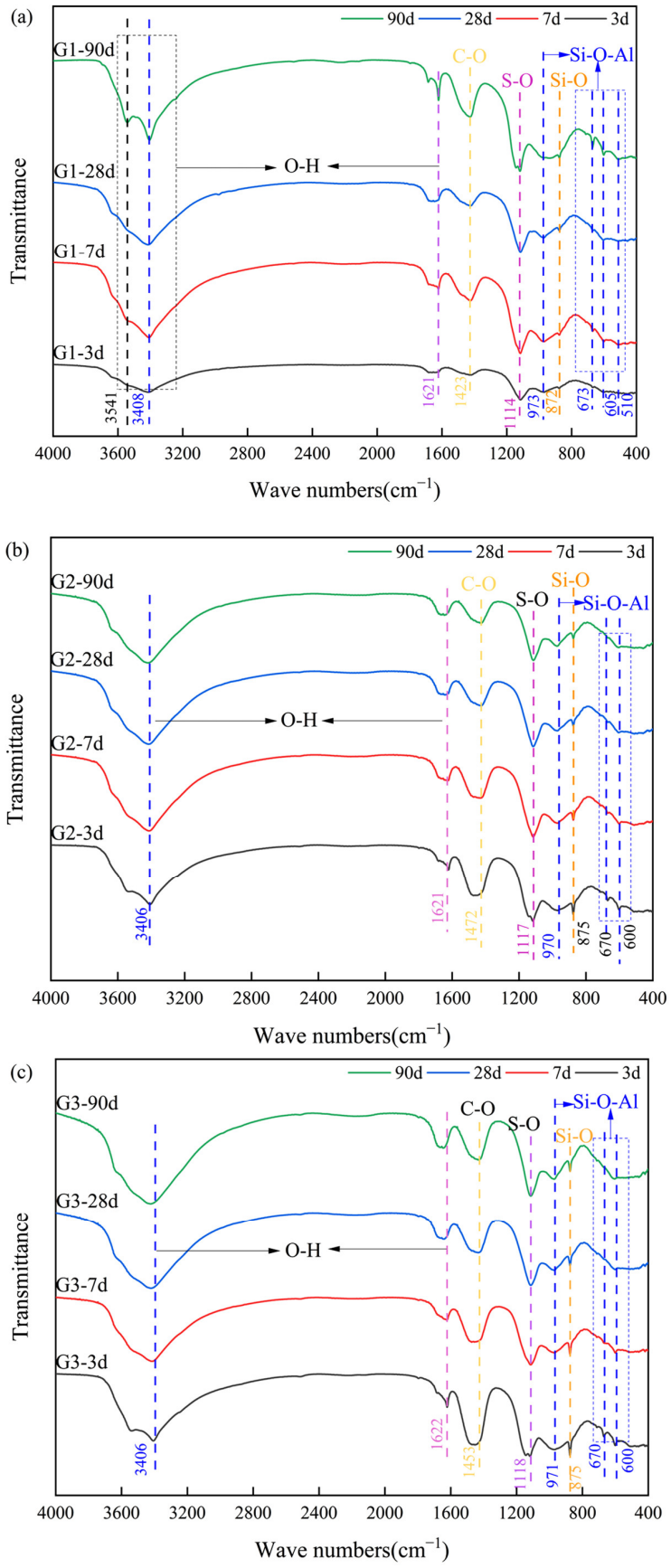


Figure 5. *Cont.*

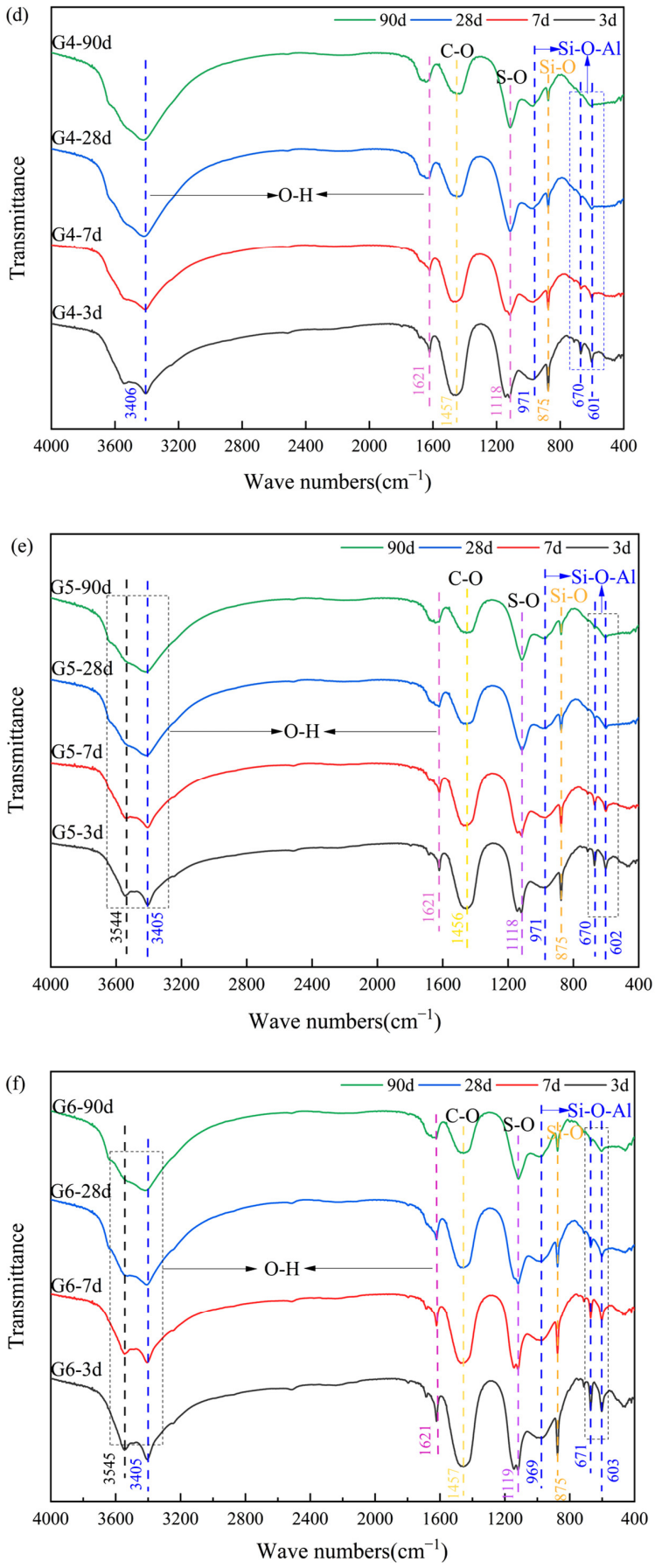


Figure 5. FT-IR spectra of the quaternary binder systems at different curing ages: (**a**) G1; (**b**) G2; (**c**) G3; (**d**) G4; (**e**) G5; (**f**) G6.

2.3.4. TG-DTG Analysis

Figure 6 shows that the TG-DTG curves of the quaternary binder systems exhibited several characteristic mass-loss regions associated with the thermal decomposition of hydration products. All mixtures exhibited three main mass-loss regions during heating, namely 40–110 °C, 110–180 °C, and 600–800 °C, which can be assigned primarily to the dehydration of C-(A)-S-H gel, the dehydration of ettringite, and the dehydroxylation of $CaCO_3$, respectively [22–24]. In particular, the mass loss at approximately 100–110 °C is mainly associated with the dehydration of ettringite and C-(A)-S-H gel. The DTG signal around 136 °C may be attributed to the overlapping dehydration of sulfate-bearing hydrates, including ettringite and residual calcium sulfate hydrate derived from FGDG [25]. The mass loss in the 500–600 °C range was attributed to the further dehydroxylation of structurally bound water in C-(A)-S-H/C-S-H-type hydrates [26].

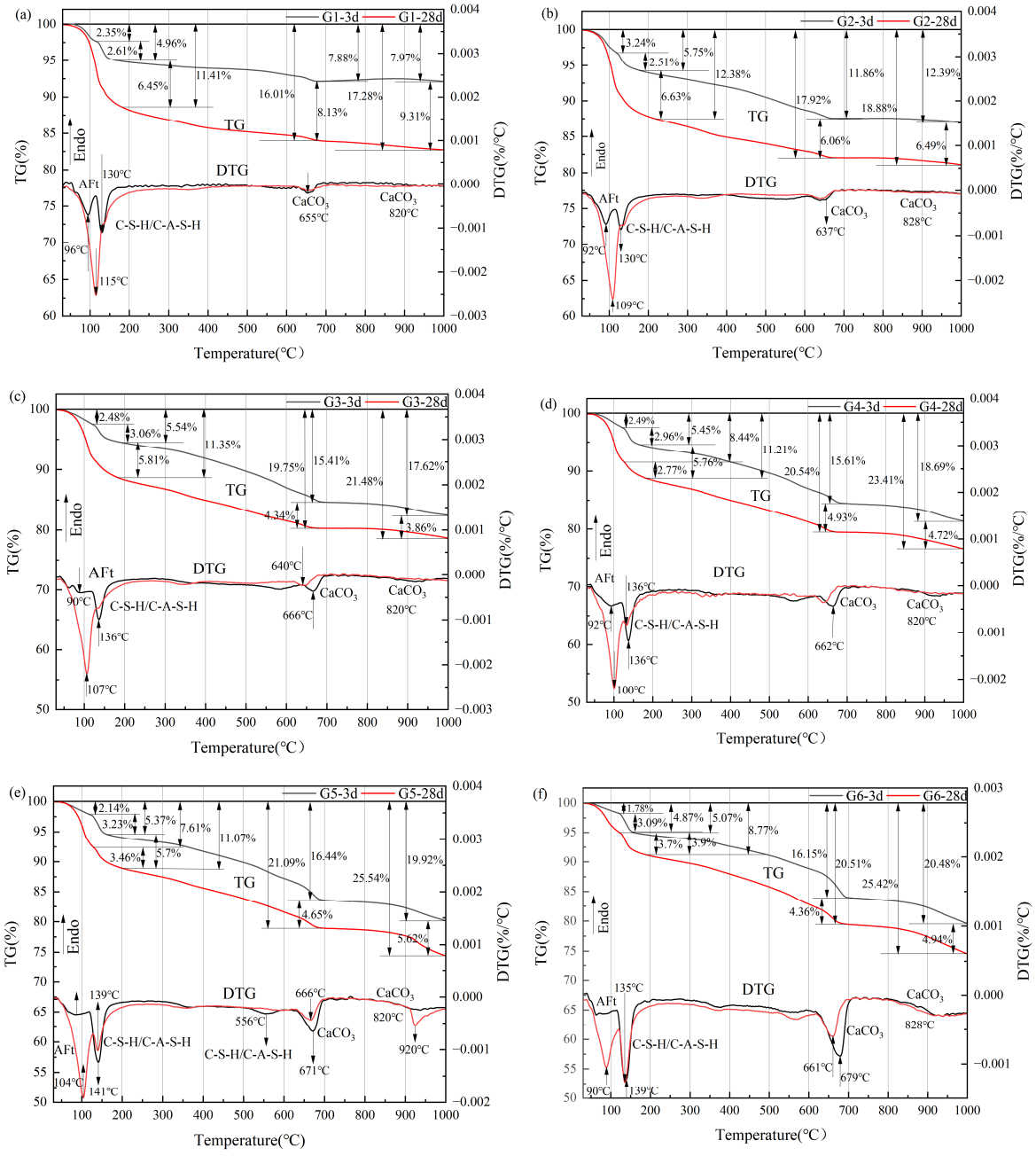


Figure 6. TG-DTG curves of the quaternary binder systems at different curing ages: (**a**) G1; (**b**) G2; (**c**) G3; (**d**) G4; (**e**) G5; (**f**) G6.

With increasing curing age, the low-temperature mass loss became more pronounced, indicating the continuous formation of hydration products. Among the mixtures, G3 exhibited the most evident increase in the 40–180 °C mass loss, suggesting that a moderate MSWI fly ash dosage promoted the formation of ettringite and C-(A)-S-H gel. This result agrees with the XRD and FT-IR observations, in which stronger ettringite reflections and more evident Si-O/Si-O-Al vibration bands were observed for the optimized mixture. In contrast, the weaker low-temperature mass loss of G6 indicates that excessive MSWI fly ash did not effectively contribute to hydrate accumulation, which is consistent with its lower strength development.

The mass loss in the high-temperature range of approximately 630–670 °C should be attributed to the decarbonation of minor carbonate-containing phases, mainly $CaCO_3$. The presence of carbonate species was also supported by the carbonate-related FT-IR bands at approximately 875 cm^{-1}. These carbonate phases may have originated from slight surface carbonation during curing, drying, or sample handling.

Figure 7 further compares the TG-DTG curves of the representative G1, G3, and G6 mixtures to clarify the effect of MSWI fly ash dosage on hydrate accumulation. At 3 d, the total mass loss in the 40–180 °C range followed the order G3 > G1 > G6. This temperature region is mainly associated with the dehydration of C-(A)-S-H gel, ettringite, and sulfate-bearing hydrates, indicating that a moderate MSWI fly ash dosage promoted early hydrate formation. The higher mass loss of G3 suggests that MSWI fly ash enhanced the alkaline activation of low-titanium slag and accelerated the conversion of dissolved Ca, Si, and Al species into hydration products. At 28 d, the low-temperature mass loss remained highest for G3, followed by G1 and G6. This result indicates that the optimized MSWI fly ash dosage supported sustained hydrate accumulation during curing, whereas excessive MSWI fly ash weakened effective hydration. The lower mass loss of G6 reflects the insufficient formation of strength-contributing hydrates, which is consistent with its lower compressive strength and less developed microstructure.

2.3.5. XPS Analysis

Figure 8 presents the XPS spectra of the representative G3 system at 3 and 28 d, showing clear curing-age-dependent shifts in the chemical states of the major elements. The Ca 2p binding energy increased slightly from 347.17 to 347.20 eV, indicating the continuous incorporation of Ca into newly formed hydration products. The Si 2p binding energy shifted from 101.58 to 101.81 eV, indicating progressive reconstruction of the silicate environment and the development of a more polymerized C-(A)-S-H structure [27,28]. A similar positive shift was observed for Al 2p, from 73.98 to 74.07 eV, suggesting a gradual increase in the proportion of more stable octahedrally coordinated Al relative to less ordered tetrahedral Al environments, which is consistent with the formation of ettringite and other Al-bearing hydrates [29,30]. Meanwhile, the O 1s binding energy increased from 531.49 to 531.68 eV, confirming the increasing degree of oxygen bonding order and silicate network polymerization during hydration. The Ti 2p and S 2p spectra further support this evolution. Ti 2p shifted from 458.07 to 459.05 eV, indicating gradual structural reorganization of Ti-bearing phases inherited from low-titanium slag, while S 2p increased from 168.81 to 168.96 eV, reflecting the stabilization of sulfate in more ordered hydration products, especially ettringite [31,32]. Taken together, these systematic positive shifts demonstrate that the G3 system underwent continuous Ca-Si-Al-S chemical reconstruction from 3 to 28 d, leading to higher hydrate polymerization, more stable Al coordination, and a denser reaction network. This provides direct spectroscopic evidence that the optimum MSWI fly ash dosage promotes not only early activation, but also the sustained development of a chemically more ordered and mechanically stronger hydrate structure.

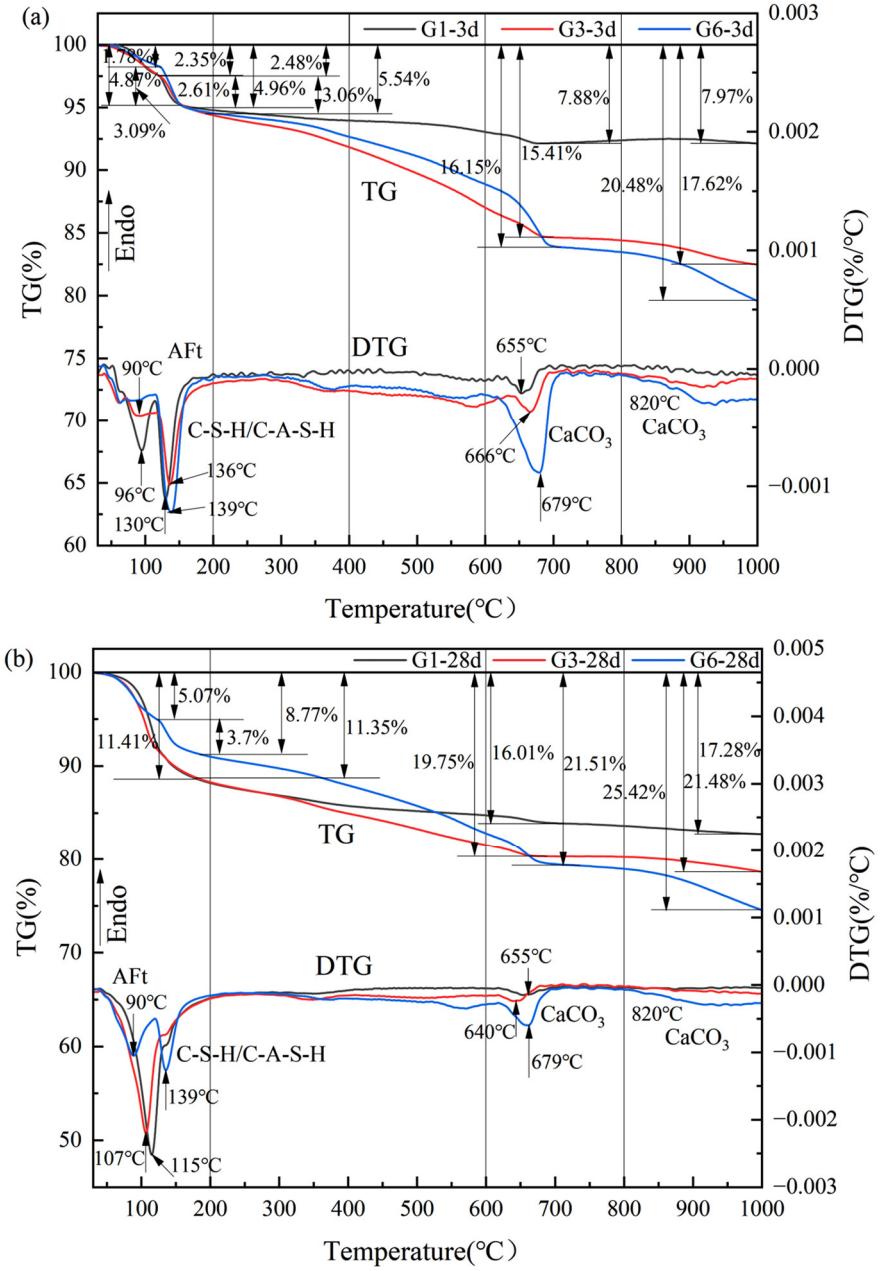


Figure 7. TG-DTG comparison of selected quaternary binder systems at different curing ages: (**a**) 3 d; (**b**) 28 d.

2.3.6. SEM Analysis

Figure 9 shows the microstructural evolution of the representative G3 paste at 3, 7, and 28 d. At 3 d, only a limited amount of hydration products was observed, and the matrix exhibited a loose and porous morphology dominated by fine particulate agglomerates. Sparse needle-like ettringite and a small amount of primary C-(A)-S-H gel could be identified, providing only weak initial structural support between unreacted particles. This explains the relatively low compactness and strength at the early stage. At 7 d, the amount of ettringite and C-(A)-S-H gel increased markedly, and the microstructure became significantly denser. Ettringite developed from fine needles into short rod-like crystals, while the newly formed C-(A)-S-H gel progressively filled intercrystalline voids and coated residual particles, resulting in a much more integrated hydrate framework. By 28 d, the hydration products had accumulated substantially, and the matrix evolved into a compact multi-scale composite structure. Ettringite further grew into well-developed elongated

crystals and was closely intergrown with abundant C-(A)-S-H gel, which continuously filled pores and strengthened interfacial bonding. In addition, plate-like Friedel's salt was observed, indicating the chemical incorporation of chloride into stable hydration products. Therefore, the SEM results confirm that the superior performance of G3 originates from the progressive establishment of a coupled hydrate framework composed of ettringite, C-(A)-S-H gel, and Friedel's salt, which simultaneously enhances structural densification, strength development, and chloride stabilization.

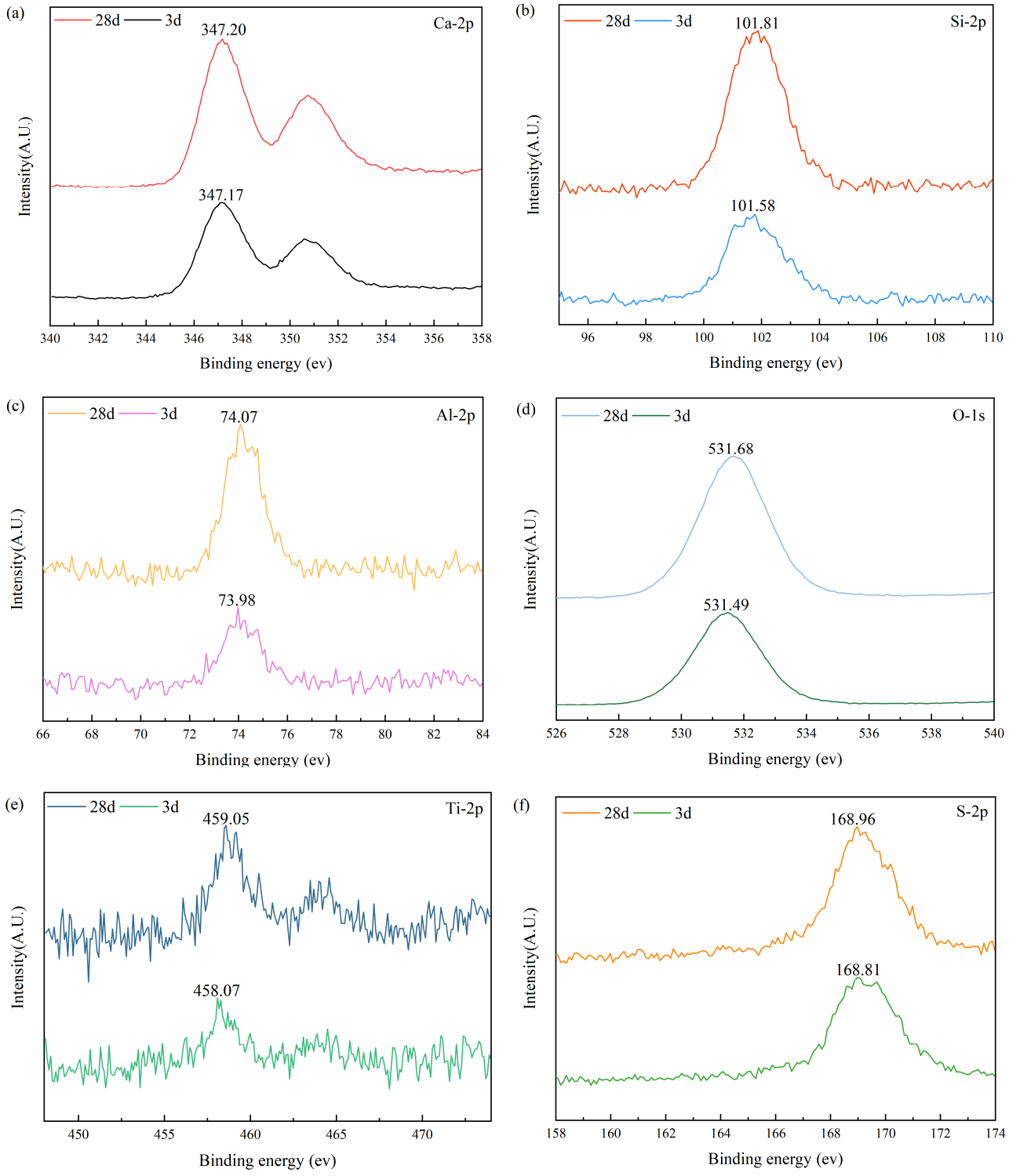


Figure 8. XPS spectra of the representative G3 sample at different curing ages: (**a**) Ca 2p; (**b**) Si 2p; (**c**) Al 2p; (**d**) O 1s; (**e**) Ti 2p; (**f**) S 2p.

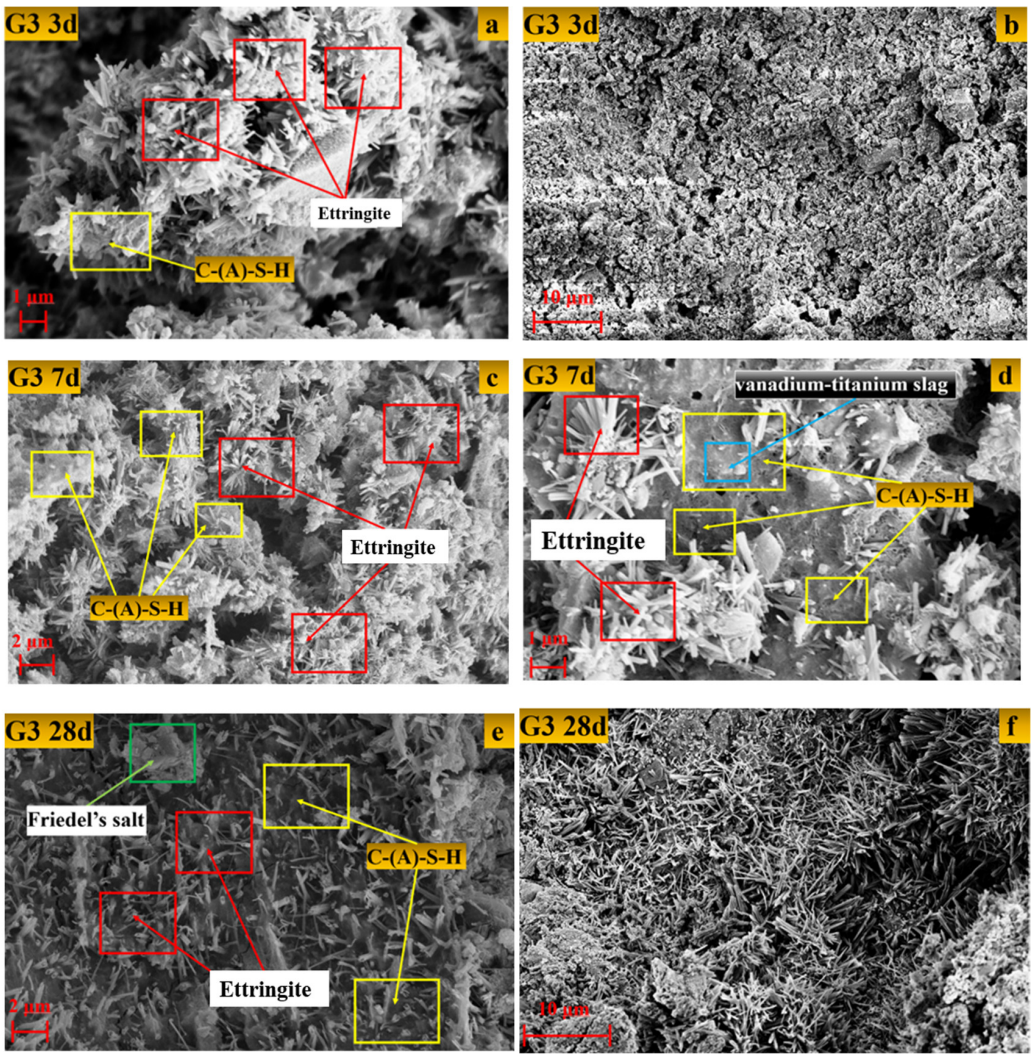


Figure 9. SEM images of the representative G3 sample at different curing ages: (**a**) G3-3d; (**b**) G3-3d; (**c**) G3-7d; (**d**) G3-7d; (**e**) G3-28d; (**f**) G3-28d.

2.4. Hydration Process of the MSWI Fly Ash-Low-Titanium Slag-Based Cementitious Materials

The hydration of the MSWI fly ash-low-titanium slag-based quaternary binder is mainly controlled by the activation effect of MSWI fly ash on the low-reactivity Ca-Si-Al network of low-titanium slag. At the early stage, MSWI fly ash and steel slag released Ca-rich alkaline species, which increased the alkalinity of the reaction environment and promoted the initial dissolution of low-titanium slag [33,34]. This process was reflected by the enhanced early heat-flow response of the mixtures with moderate MSWI fly ash addition, which is consistent with the accelerated dissolution and hydration behavior commonly observed in alkali-activated slag-based binders [35]. Meanwhile, sulfate supplied by FGDG reacted with the dissolved Ca and Al species, leading to the preferential formation of ettringite and the establishment of an early hydration framework [36]. As hydration proceeded, the continuous depolymerization of the low-titanium slag provided additional silicate and aluminate species [37]. This interpretation is supported by the development of the amorphous hump in XRD patterns, the evolution of Si-O and Si-O-Al vibration bands in FT-IR spectra, and the increased low-temperature dehydration signals in TG-DTG curves. The shifts in Ca, Si, Al, O, and S binding energies further indicated the progressive reconstruction of the Ca-Si-Al-S chemical environment during curing, since XPS binding-energy variations are closely associated with changes in silicate polymerization and the local chemical environment of calcium silicate hydrate-type phases [38,39]. Consequently,

ettringite contributed mainly to early structural build-up, whereas C-(A)-S-H gel gradually filled pores and improved the later-age compactness of the matrix, as observed from SEM images. Friedel's salt was also identified as a chloride-bearing AFm phase associated with the chloride-containing MSWI fly ash system, which is consistent with the established chloride-binding behavior of AFm phases in cementitious materials [40,41].

This evolution also explains the strength development of the optimized mixture. The higher cumulative heat release of G3 reflected a more sustained hydration process, while the stronger XRD and FT-IR signals and the increased low-temperature mass loss in TG-DTG indicated greater accumulation of ettringite and C-(A)-S-H gel. These hydration products filled interparticle voids and improved the continuity of the hardened matrix, thereby contributing to the higher compressive strength. In contrast, the weaker heat release and lower hydrate-related signals of G6 corresponded to insufficient hydrate accumulation and a less compact microstructure, which was consistent with its reduced strength development. Therefore, an appropriate dosage of MSWI fly ash promoted slag activation and hydrate formation by regulating the alkaline reaction environment and ion supply, while excessive MSWI fly ash weakened effective hydration, probably due to an unfavorable imbalance among Ca-rich species, chloride-bearing components, and reactive Si-Al sources, thereby limiting the continuous formation of ettringite and C-(A)-S-H gel [42]. It should be noted that MSWI fly ash composition may vary significantly depending on waste source and incineration conditions, especially in terms of chloride, soluble salts, and heavy metals [42,43]. Such variability may affect the activation efficiency, hydrate assemblage, and environmental applicability of the binder system. Future work will therefore evaluate MSWI fly ashes with different chemical compositions to further verify the robustness and engineering adaptability of the proposed quaternary binder.

3. Materials and Methods

In this study, four representative industrial solid wastes were used as raw materials, including low-titanium slag (LTS), steel slag (SS), municipal solid waste incineration fly ash (MSWI fly ash), and flue-gas desulfurization gypsum (FGDG), all of which were supplied by a steel plant in Guizhou, China. Prior to use, LTS, SS, and FGDG were mechanically ground using an SMΦ500 × 500 laboratory ball mill to obtain sufficient fineness for subsequent binder reactions. All materials were oven-dried and stored in sealed containers before mixing. The chemical compositions of the raw materials, as presented in Table 2, were determined using a wavelength-dispersive X-ray fluorescence spectrometer (WD-XRF, XRF-1800, Shimadzu, Kyoto, Japan). LTS is rich in Ca, Si, and Al, indicating its potential as a reactive slag precursor for the generation of aluminosilicate hydrate phases. The relatively high CaO contents of SS and MSWI fly ash favor the rapid release of calcium species during the initial reaction stage, which contributes to an increase in Ca^{2+} availability in the pore solution and thus accelerates slag dissolution and hydrate formation. FGDG mainly provides sulfate and calcium sources, playing a key role in regulating the reaction route and phase assemblage of the system. The particle-size distribution and basic physicochemical properties of the same raw materials had been systematically characterized in our previous study [44].

A quaternary binder system composed of low-titanium slag, steel slag, MSWI fly ash, and FGDG was designed to evaluate the activating effect of MSWI fly ash on low-titanium slag. The mixture levels were selected based on our previous study [44], in which this formulation exhibited excellent workability and mechanical performance. The corresponding mix proportions are presented in Table 3. The water-to-binder ratio was fixed at 0.32 for all mixtures. After weighing according to the designed proportions, the raw materials were mechanically mixed to obtain homogeneous pastes and then cast into

30 × 30 × 50 mm molds. The specimens were cured at 20 °C and 98% relative humidity, demolded after approximately 24 h, and maintained under the same conditions until the designated testing ages. Compressive strength was determined at 3, 7, 28, and 90 d, with three parallel specimens prepared for each mixture.

Table 2. Chemical composition of raw materials.

Raw Materials	CaO	SiO_2	Al_2O_3	TiO_2	MgO	SO_3	Fe_2O_3	MnO	Na_2O	Cl	LOL
LTS	43.82	26.43	12.29	6.11	5.21	2.45	1.64	0.76	0.61	0.02	0.66
SS	45.03	11.76	1.35	3.41	4.43	1.79	26.11	4.43	0.03	0.04	1.62
MSWI fly ash	52.89	7.12	3.49	0.02	2.76	5.74	1.39	0.05	7.68	17.4	1.72
FGDG	52.77	1.79	0.34	0.22	0.26	43.12	0.42	0.13	0.11	0.56	0.41

Table 3. Mix Proportion Design of Low-Titanium Slag-Based Cementitious System.

Sample	MSWI Fly Ash	SS	LTS	FGDG	MSWI Fly Ash Replacement Ratio
	/wt. %				/%
G1	0	43.0	43	14	0
G2	8.6	34.4	43	14	20
G3	17.2	25.8	43	14	40
G4	25.8	17.2	43	14	60
G5	34.4	8.6	43	14	80
G6	43	0	43	14	100

The efficacy coefficient method was adopted to determine the optimum MSWI fly ash dosage for preparing the MSWI fly ash-low-titanium slag-based quaternary cementitious material. This method has been widely used for multi-index optimization of cementitious materials and concrete mixtures [45,46]. In this study, the compressive strengths of G1-G6 at 3, 7, 28, and 90 d were selected as the performance evaluation indicators. In this study, the compressive strengths at 3, 7, 28, and 90 d were assigned equal weight in the efficacy coefficient analysis. The overall efficacy coefficient was calculated using the geometric mean of the four individual efficacy coefficients, thereby reflecting the balanced strength development of each mixture across different curing ages. A lower efficacy coefficient at any curing age would reduce the final overall efficacy coefficient. For each curing age, the maximum compressive strength was assigned an efficacy coefficient of 1, and the efficacy coefficients of the other mixtures were calculated as the ratio of their measured strength to the corresponding maximum strength. The overall efficacy coefficient was then calculated as the geometric mean of the four individual efficacy coefficients, thereby reflecting the comprehensive contribution of strength development at different curing ages. The mixture with the highest overall efficacy coefficient was considered to have the best comprehensive mechanical performance. Since all indices belonged to the larger-the-better type, the efficacy coefficient for each index was calculated as the ratio of the measured value to the maximum value obtained at the same curing age, as expressed in Equation (1):

$$d_i = \frac{x_i}{x_{i,\max}} \quad (1)$$

where d_i is the efficacy coefficient of the compressive strength at a given curing age, x_i is the measured compressive strength of a given mixture at that curing age, and $x_{i,\max}$ is the maximum compressive strength among all mixtures at the same curing age. In this study, d_1, d_2, d_3 and d_4 correspond to the efficacy coefficients at 3, 7, 28, and 90 d, respectively.

To reflect the overall mechanical performance over the entire curing period, the overall efficacy coefficient D was calculated as the geometric mean of the four individual efficacy coefficients, as given in Equation (2):

$$D = \sqrt[4]{d_1 \cdot d_2 \cdot d_3 \cdot d_4} \quad (2)$$

A higher D value indicates a better overall balance of compressive strength at different curing ages. Based on this method, the optimum mixture proportion was identified by jointly considering early-age strength, long-term strength, and the utilization level of MSWI fly ash.

The chemical compositions of the raw materials were determined by X-ray fluorescence spectroscopy (XRF, XRF-1800, Beijing Huarda Science and Technology Co., Ltd., Beijing, China). The phase assemblages of hydrated samples were identified by X-ray diffraction (XRD, Ultima IV, Rigaku, Japan) with Cu Kα radiation at 40 kV and 10 mA over a 2θ range of 5–90 degrees, using a step size of 0.02 degrees and a scanning rate of 5 degrees/min. Fourier transform infrared spectroscopy (FT-IR, Nicolet iS20, Thermo Fisher Scientific, Waltham, MA, USA) was used to characterize the evolution of functional groups and bonding structures in the range of 400–4000 cm^{-1} with a resolution of 4 cm^{-1}. Thermogravimetric and derivative thermogravimetric analyses (TG-DTG) were performed using a simultaneous thermal analyzer (STA 449 F3, Netzsch, Selb, Germany) from 30 to 1000 °C under a high-purity Ar atmosphere at a heating rate of 10 °C/min to examine the thermal decomposition behavior of the hydration products. X-ray photoelectron spectroscopy (XPS, K-Alpha, Thermo Scientific, USA) was further employed to investigate the evolution of elemental chemical states in the hydrated binders. The hydration behavior was evaluated by isothermal calorimetry (TAM Air, TA Instruments, New Castle, DE, USA), in which paste samples with a water-to-binder ratio of 0.32 were monitored for 168 h to obtain the heat flow and cumulative heat release. In addition, the micromorphology of the hydration products was examined using a scanning electron microscope equipped with energy-dispersive spectroscopy (SEM-EDS, FEI Quanta 650, FEI, Hillsboro, OR, USA) at an accelerating voltage of 10 kV, with a spot size of 6 and an aperture size of 3.

4. Conclusions

This study clarified the dosage-dependent role of MSWI fly ash in activating a low-titanium-slag-based quaternary cementitious material and revealed its effects on compressive strength development, hydration heat evolution, hydrate formation, and microstructural reconstruction. The results confirm that an appropriate amount of MSWI fly ash can effectively promote low-titanium slag activation and the coordinated formation of strength-contributing hydration products.

(1) The compressive strength showed a clear increase-then-decrease trend with increasing MSWI fly ash content, indicating that the activating effect of MSWI fly ash was effective only within an appropriate dosage range. Based on the combined evaluation of compressive strength at different curing ages using the efficacy coefficient method, the optimum formulation was determined as low-titanium slag:MSWI fly ash:steel slag:FGDG = 43.0:17.2:25.8:14.0. This mixture achieved compressive strengths of 9.51 MPa at 3 d and 46.32 MPa at 90 d. The optimized binder exhibited effective activation and shows potential for non-structural low-carbon cementitious applications, such as cemented paste backfill. However, its broader engineering use still requires further validation of volumetric stability, durability, and leaching safety.

(2) Moderate MSWI fly ash incorporation increased the heat flow and cumulative heat release during the main hydration stage and promoted sustained hydrate formation.

In contrast, excessive MSWI fly ash reduced the cumulative heat release and weakened later hydration.

(3) XRD, FT-IR, TG-DTG, XPS, and SEM analyses consistently showed that ettringite, C-(A)-S-H gel, and Friedel's salt were the main hydration products controlling the performance of the system. The optimized mixture exhibited greater hydrate accumulation, higher gel polymerization, and a denser microstructure, whereas excessive MSWI fly ash reduced effective hydrate formation and deteriorated structural compactness.

(4) The hydration of the quaternary system was governed by the synergistic coupling of Ca supply, sulfate activation, and aluminosilicate depolymerization. Steel slag and MSWI fly ash provided Ca-rich alkaline components, FGDG supplied sulfate, and low-titanium slag continuously released reactive Si and Al species to form ettringite and C-(A)-S-H gel. The key role of MSWI fly ash was to regulate low-titanium slag activation and hydrate evolution; at an appropriate dosage it promoted hydration, whereas excessive addition disturbed the Ca-Si-Al balance and suppressed effective gel formation.

Author Contributions: Conceptualization B.S. and J.C.; Data curation, B.S.; Formal analysis, B.S.; Methodology, B.S.; Writing—original draft preparation, B.S.; Conceptualization, J.C.; Supervision S.Z., K.L. and W.N.; Resources, S.Z.; Validation, J.L. and X.X. All authors have read and agreed to the published version of the manuscript.

Funding: This research was funded by Guizhou Provincial Science and Technology Program Project, grant number Qian Ke He Zhong Yin Di (2025) 011.

Data Availability Statement: The original contributions presented in this study are included in the article. Further inquiries can be directed to the corresponding author.

Conflicts of Interest: The authors declare no conflicts of interest.

References

1. Guo, Y.; Luo, L.; Liu, T.; Hao, L.; Li, Y.; Liu, P.; Zhu, T. A review of low-carbon technologies and projects for the global cement industry. *J. Environ. Sci.* **2024**, *136*, 682–697. [CrossRef] [PubMed]
2. Li, X.; Sun, Y.; Li, W.; Nie, Y.; Wang, F.; Bian, R.; Wang, H.; Wang, Y.-N.; Gong, Z.; Lu, J.; et al. Solidification/stabilization pre-treatment coupled with landfill disposal of heavy metals in MSWI fly ash in China: A systematic review. *J. Hazard. Mater.* **2024**, *478*, 135479. [CrossRef] [PubMed]
3. Zhang, Y.; Wang, L.; Chen, L.; Ma, B.; Zhang, Y.; Ni, W.; Tsang, D.C.W. Treatment of municipal solid waste incineration fly ash: State-of-the-art technologies and future perspectives. *J. Hazard. Mater.* **2021**, *411*, 125132. [CrossRef]
4. Xia, Y.; Liu, Z.; Song, Z.; Zhao, R.; Wu, J.; Wang, L.; Yan, J. Valorization of municipal solid waste incineration fly ash in low-carbon alkali-activated materials. *Chem. Eng. J.* **2024**, *495*, 153577. [CrossRef]
5. Paul, G.; Boccaleri, E.; Buzzi, L.; Canonico, F.; Gastaldi, D. Friedel's salt formation in sulfoaluminate cements: A combined XRD and ^{27}Al MAS NMR study. *Cem. Concr. Res.* **2015**, *67*, 93–102. [CrossRef]
6. Yang, D.; Kow, K.-W.; Wang, W.; Meredith, W.; Zhang, G.; Mao, Y.; Xu, M. Co-treatment of municipal solid waste incineration fly ash and alumina-/silica-containing waste: A critical review. *J. Hazard. Mater.* **2024**, *479*, 135677. [CrossRef]
7. Cao, L.; Zuo, Y.; Liang, S.; Sun, Y.; Ke, Y.; Yang, J.; Wei, X.; Hu, J.; Hou, H. Geopolymerization of MSWI fly ash and coal fly ash for efficient solidification of heavy metals: Insights into stabilization mechanisms and long-term leaching behavior. *Constr. Build. Mater.* **2024**, *411*, 134359. [CrossRef]
8. Qu, Y.; Xing, L.; Gao, M.; Zhao, S.; Ren, Q.; Li, L.; Long, Y. Progress and Prospects for Titanium Extraction from Titanium-Bearing Blast Furnace Slag. *Materials* **2024**, *17*, 6291. [CrossRef]
9. Tao, M.; Lu, D.; Shi, Y.; Wu, C. Utilization and life cycle assessment of low activity solid waste as cementitious materials: A case study of titanium slag and granulated blast furnace slag. *Sci. Total Environ.* **2022**, *849*, 157797. [CrossRef]
10. Zhao, Y.; Zhou, X.; Zhou, Q.; Zhu, H.; Cheng, F.; Chen, H. Development of full-solid waste environmentally binder for cemented paste backfill. *Constr. Build. Mater.* **2024**, *443*, 137689. [CrossRef]
11. Wang, J.; Xiao, B.; Liu, X.; Ruan, Z. Trends and Applications of Green Binder Materials for Cemented Paste Backfill Mining in China. *Minerals* **2025**, *15*, 97. [CrossRef]
12. Wang, S.; Zhu, G.; Pu, X. Study on Cementitious Properties and Hydration Characteristics of Steel Slag. *Pol. J. Environ. Stud.* **2018**, *27*, 357–364. [CrossRef]

13. Sanderson, R.A.; Cann, G.M.; Provis, J.L. Comparison of calorimetric methods for the assessment of slag cement hydration. *Adv. Appl. Ceram.* **2017**, *116*, 186–192. [CrossRef]
14. Xu, Z.; Li, J.; Zhang, Y.; Huang, S.; Li, H. Preparation and Hydration Properties of Steel Slag-Based Composite Cementitious Materials with High Strength. *Materials* **2023**, *16*, 2764. [CrossRef] [PubMed]
15. Araos, P.; Aponte, D.; Barra, M. Ladle furnace slag as a new source of supplementary cementitious material: Evaluating long-term performance and environmental impact in Portland cement systems. *J. Build. Eng.* **2024**, *95*, 109995. [CrossRef]
16. Torrens-Martín, D.; Fernández-Carrasco, L. Impact of calcium aluminate cement and calcium sulfate on gel C-A-S-H formation during the Portland cement hydration. *Mater. Construcc.* **2025**, *75*, e397. [CrossRef]
17. He, H.; Gao, Y.; Yu, J.; Zhang, W.; Shen, X.; Zhang, M. Municipal solid waste incineration fly ash as activator for ground granulated blast-furnace slag: Hydration behavior and stabilization/solidification effectiveness. *Case Stud. Constr. Mater.* **2025**, *23*, e05177. [CrossRef]
18. Perez-Cortes, P.; Garcia-Lodeiro, I.; Alonso, M.C.; Puertas, F. Cementation of spent radioactive ion-exchange resin ashes using alkali-activated cements: Physicochemical and structural changes. *Cem. Concr. Compos.* **2024**, *149*, 105517. [CrossRef]
19. Vázquez-Rodríguez, F.J.; Torre, A.G.D.L.; Santacruz, I.; Matschei, T.; Álvarez-Pinazo, G. The Effect of μ-Limestone Additions on the Mechano-Chemical Activation of Ladle Slag. *Materials* **2024**, *17*, 5940. [CrossRef]
20. Yang, J.; Hou, D.; Wang, P.; Zhang, L.; Yu, J.; Wang, P. Synthesis of Nanoscale CaO-Al_2O_3-SiO_2-H_2O and Na_2O-Al_2O_3-SiO_2-H_2O Using the Hydrothermal Method and Their Characterization. *Materials* **2017**, *10*, 695. [CrossRef] [PubMed]
21. Santos, V.H.J.M.d.; Pontin, D.; Ponzi, G.G.D.; Stepanha, A.S.d.G.e.; Martel, R.B.; Schütz, M.K.; Einloft, S.M.O.; Dalla Vecchia, F. Application of Fourier Transform infrared spectroscopy (FTIR) coupled with multivariate regression for calcium carbonate ($CaCO_3$) quantification in cement. *Constr. Build. Mater.* **2021**, *313*, 125413. [CrossRef]
22. Alarcon-Ruiz, L.; Platret, G.; Massieu, E.; Ehrlacher, A. The use of thermal analysis in assessing the effect of temperature on a cement paste. *Cem. Concr. Res.* **2005**, *35*, 609–613. [CrossRef]
23. Vogler, N.; Drabetzki, P.; Lindemann, M.; Kühne, H.-C. Description of the concrete carbonation process with adjusted depth-resolved thermogravimetric analysis. *J. Therm. Anal. Calorim.* **2022**, *147*, 6167–6180. [CrossRef]
24. Bílek, V.; Švec, J.; Másilko, J.; Sedlačík, M.; Materak, K.; Wieczorek, A.; Koniorczyk, M.; Hajzler, J.; Kucharczyková, B. Comparison of thermogravimetry response of alkali-activated slag and Portland cement pastes after stopping their hydration using solvent exchange method. *J. Therm. Anal. Calorim.* **2025**, *150*, 1013–1037. [CrossRef]
25. Song, H.; Jeong, Y.; Bae, S.; Jun, Y.; Yoon, S.; Oh, J.E. A study of thermal decomposition of phases in cementitious systems using HT-XRD and TG. *Constr. Build. Mater.* **2018**, *169*, 648–661. [CrossRef]
26. Im, S.; Jee, H.; Suh, H.; Kanematsu, M.; Morooka, S.; Koyama, T.; Nishio, Y.; Machida, A.; Kim, J.; Bae, S. Temperature effects on local structure, phase transformation, and mechanical properties of calcium silicate hydrates. *J. Am. Ceram. Soc.* **2021**, *104*, 4803–4818. [CrossRef]
27. Chen, B.; Hou, P.; Han, R.; Li, N.; Zhang, G.; Shah, S.P. Molecular elucidation of cement hydration inhibition by silane molecules. *Nat. Commun.* **2025**, *16*, 2290.
28. Xing, X.; Cao, M.; Lv, S.; Ma, Y.; Wang, H.; Zhou, Y. Effect of organic polymers on mechanical property and microstructure of slag geopolymer paste. *Polymers* **2022**, *14*, 4214. [CrossRef] [PubMed]
29. Zheng, D.; Ji, T.; Wang, C.; Sun, Z.; Lin, X.; Hossain, K.M.A. Hydration Characteristics of Tricalcium Aluminate in the Presence of Nano-Silica. *Nanomaterials* **2021**, *11*, 199. [CrossRef]
30. Gasharova, B.; Rose, V.; Peterson, V.K.; Bellmann, F.; Möbus, G.; O'Neill, T.; Benning, L.G.; Provis, J.L. The Atomic-Level Structure of Cementitious Calcium Aluminate Sulfate Hydrate Phases. *J. Am. Chem. Soc.* **2020**, *142*, 21451–21466.
31. Zhang, S.; Yang, J.; Zhang, X.; Jiang, W.; Li, Y.; Wang, D. The Preparation Process and Hydration Mechanism of Filling Cementitious Materials Based on Industrial Solid Wastes. *Polymers* **2023**, *15*, 82.
32. Li, S.; Zhao, Y.; Wang, J.; Zhang, H.; Liu, Y.; Zhou, W. Mechanisms of concentration control alkali activated fly ash stabilized saline soil in seasonally frozen regions. *Sci. Rep.* **2025**, *15*, 1570. [CrossRef] [PubMed]
33. Provis, J.L.; Palomo, A.; Shi, C. Advances in understanding alkali-activated materials. *Cem. Concr. Res.* **2015**, *78*, 110–125. [CrossRef]
34. Ren, P.; Ling, T.-C. Roles of chlorine and sulphate in MSWIFA in GGBFS binder: Hydration, mechanical properties and stabilization considerations. *Environ. Pollut.* **2021**, *284*, 117175. [CrossRef] [PubMed]
35. Zhao, T.; Zhang, S.; Yang, H.; Ni, W.; Wu, Z.; Liu, Y.; Chen, X.; Guan, D. The influences of MSWI fly ash washing and blast furnace slag/bottom ash ratio on low-carbon cementitious materials. *J. Clean. Prod.* **2024**, *473*, 143547. [CrossRef]
36. Xia, Y.; Wang, L.; Zhao, R.; Wu, J.; Liu, Z.; Li, H.; Guo, B.; Yan, J. Industrial gypsum-driven in-situ ettringite formation for enhanced all-solid-waste alkali-activated materials. *Compos. Part B Eng.* **2026**, *309*, 113077. [CrossRef]
37. Bernal, S.A.; Provis, J.L.; Walkley, B.; San Nicolas, R.; Gehman, J.D.; Brice, D.G.; Kilcullen, A.R.; Duxson, P.; van Deventer, J.S.J. Gel nanostructure in alkali-activated binders based on slag and fly ash, and effects of accelerated carbonation. *Cem. Concr. Res.* **2013**, *53*, 127–144. [CrossRef]

38. Black, L.; Garbev, K.; Beuchle, G.; Stemmermann, P.; Schild, D. X-ray photoelectron spectroscopic investigation of nanocrystalline calcium silicate hydrates synthesised by reactive milling. *Cem. Concr. Res.* **2006**, *36*, 1023–1031. [CrossRef]
39. Black, L.; Garbev, K.; Gee, I. Surface carbonation of synthetic C-S-H samples: A comparison between fresh and aged C-S-H using X-ray photoelectron spectroscopy. *Cem. Concr. Res.* **2008**, *38*, 745–750. [CrossRef]
40. Birnin-Yauri, U.A.; Glasser, F.P. Friedel's salt, $Ca_2Al(OH)_6(Cl,OH)\cdot 2H_2O$: Its solid solutions and their role in chloride binding. *Cem. Concr. Res.* **1998**, *28*, 1713–1723. [CrossRef]
41. Balonis, M.; Lothenbach, B.; Le Saout, G.; Glasser, F.P. Impact of chloride on the mineralogy of hydrated Portland cement systems. *Cem. Concr. Res.* **2010**, *40*, 1009–1022. [CrossRef]
42. Luo, H.; Cheng, Y.; He, D.; Yang, E.-H. Review of leaching behavior of municipal solid waste incineration (MSWI) ash. *Sci. Total Environ.* **2019**, *668*, 90–103. [CrossRef]
43. Chen, W.-S.; Chang, F.-C.; Shen, Y.-H.; Tsai, M.-S.; Ko, C.-H. Removal of chloride from MSWI fly ash. *J. Hazard. Mater.* **2012**, *237–238*, 116–120. [CrossRef] [PubMed]
44. Su, B.; Chi, J.; Zhang, S.; Li, J.; Li, K.; Xu, X.; Ni, W. Preparation and Synergistic Activation Mechanism of Cemented Backfill Materials Utilizing MSWI Fly Ash and Low-Titanium Slag. *Materials* **2026**, *19*, 1551. [CrossRef]
45. Liu, Z.; Ni, W.; Li, Y.; Ba, H.; Li, N.; Ju, Y.; Zhao, B.; Jia, G.; Hu, W. The mechanism of hydration reaction of granulated blast furnace slag-steel slag-refining slag-desulfurization gypsum-based clinker-free cementitious materials. *J. Build. Eng.* **2021**, *44*, 103289. [CrossRef]
46. Liu, S.; Zheng, W.; Wang, Y. Utilization of waste foundry sand and fly ash in the production of steel fibre reinforced concrete. *J. Clean. Prod.* **2023**, *433*, 139872. [CrossRef]

Disclaimer/Publisher's Note: The statements, opinions and data contained in all publications are solely those of the individual author(s) and contributor(s) and not of MDPI and/or the editor(s). MDPI and/or the editor(s) disclaim responsibility for any injury to people or property resulting from any ideas, methods, instructions or products referred to in the content.